J Adv Ceram

Research Article

Synergistic improvement of flexural strength and fracture toughness in Si_3N_4 ceramics featuring high-entropy grain boundary phase

Weiming Wang, Weide Wang✉, Yiming Liu, Kuanhong Zeng, Yong Mo, Qingsong Ma✉

Cite this article: Wang W, Wang W, Liu Y, et al. *J Adv Ceram* 2026, **15**(2): 9221230. https://doi.org/10.26599/JAC.2025.9221230

ABSTRACT: Developing silicon nitride (Si_3N_4) ceramics with concurrently enhanced flexural strength and fracture toughness presents significant challenges due to the critical dependence of these macroscopic properties on microstructure. This study produced high-performance Si_3N_4 ceramics by employing multiple rare earth (RE) oxides (RE_2O_3) as sintering additives to construct a multicomponent rare earth ion liquid phase via hot pressing sintering (HPS). The designed multicomponent RE-ion liquid phase reduces the shrinkage onset temperature while facilitating densification and α→β phase transformation. Synergistic effects among the multicomponent RE-ion liquid phase foster a distinct bimodal microstructure characterized by an optimized spatial distribution of refined matrix grains interlocked with elongated rod-like β-Si_3N_4 grains exhibiting elevated aspect ratios. Concurrently, the multicomponent RE-ion liquid phase crystallizes into a high-entropy $(Gd_{0.2}Y_{0.2}Yb_{0.2}Lu_{0.2}Sc_{0.2})_2Si_2O_7$, enabling high crystallinity of the grain boundary phase in Si_3N_4 ceramics. Through concurrent optimization of microstructure and grain boundary phase properties in Si_3N_4 ceramics, synergistic enhancement in flexural strength (1322 MPa) and fracture toughness (10.88 MPa·m$^{1/2}$) is achieved. Collectively, this high-entropy approach establishes a highly promising transformative strategy for developing high-performance structural ceramics.

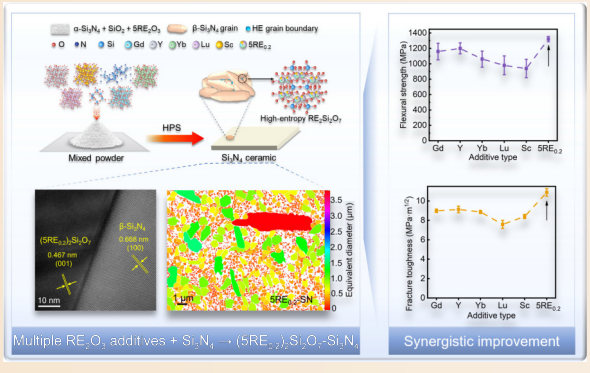

KEYWORDS: silicon nitride (Si_3N_4) ceramics; liquid phase sintering; high-entropy rare earth (RE) disilicate; grain boundary phase; mechanical properties

1 Introduction

Silicon nitride (Si_3N_4) ceramics have garnered significant attention as structural materials due to their exceptional combination of properties, including high strength, excellent toughness, remarkable hardness, and superior wear resistance. These characteristics make it an ideal candidate for demanding applications across aerospace, automotive, electronics, and medical industries [1–4]. However, achieving the coordinated development of diverse mechanical properties in Si_3N_4 ceramics is challenging due to the pronounced correlation of macroscopic mechanical performance to microstructure. Flexural strength is enhanced by a fine-grained microstructure through grain refinement strengthening [5,6], while fracture toughness relies on the presence of large, elongated β-Si_3N_4 grains that enable crack deflection, crack bridging, and grain pull-out [7].

A proven strategy to resolve this conflict is to design a bimodal microstructure, where sparse, large elongated grains are uniformly dispersed within a fine-grained matrix [8]. This microstructure design strategy is implemented primarily through two approaches. First, the introduction of β-Si_3N_4 seeds as heterogeneous nucleation sites promotes the development of large elongated grains. By optimizing the size and amount of these seeds, researchers have successfully obtained well-dispersed high-aspect-ratio β-Si_3N_4 grains, leading to improved fracture toughness without a significant loss of strength [9–11]. Second, as densification, phase transformation, and grain growth are mediated by the liquid phase during sintering, careful selection of sintering additives enables the decoupling of β-Si_3N_4 nucleation from densification [12]. For example, controlling the nitrogen-to-oxygen ratio via oxygen-free additives can suppress densification at lower temperatures while permitting phase transformation, thereby facilitating bimodal microstructure development upon subsequent heating [13–15]. Additionally, the ratio of rare earth oxides (RE_2O_3) to alkaline earth elements in additives influences the process; higher Al_2O_3 content promotes densification, whereas increased Y_2O_3 favors phase transformation [16]. RE elements significantly affect phase evolution, densification, and

College of Aerospace Science and Engineering, National University of Defense Technology, Changsha 410073, China.

✉ Corresponding authors. E-mail: W. Wang, nudtwwd@163.com; Q. Ma, nudtmqs1975@163.com

Received: September 15, 2025; Revised: November 27, 2025; Accepted: December 12, 2025

microstructure development. The RE-ion radius directly influences the liquid phase viscosity and interfacial bonding. A smaller RE-ion radius increases viscosity, hindering the dissolution-precipitation process necessary for β-Si_3N_4 growth, while a larger radius enhances adsorption between RE atoms and nitrogen on the (0001) plane [17–19].This dual dependence on ionic radius creates competing effects in microstructural evolution [20–24]. Consequently, larger RE ions lower the α→β transformation temperature and encourage high-aspect-ratio grain morphology, improving fracture toughness [25,26]. However, excessively large RE ions may lead to overgrown grains and critical flaws, reducing the flexural strength [27–29]. Recent studies show that binary RE_2O_3 additives produce synergistic effects, offering over 10% improvement in self-reinforcement and toughening compared to single-component systems [30]. These multicomponent RE-ion liquid phases, with tailored ionic radius differences and moderate average radii, effectively promote optimized bimodal microstructures.

Furthermore, the grain boundary phase significantly influences both the flexural strength and fracture toughness of Si_3N_4 ceramics. After liquid phase cooling, sintering additives partially crystallize within the grain boundary phase. Their higher thermal expansion coefficient induces residual tensile stress in Si_3N_4 grains, promoting a transition from transgranular to intergranular fracture, which enhances fracture toughness [31,32]. Regarding flexural strength, the low strength of the grain boundary glassy phase reduces the overall strength. Promoting its crystallization strengthens the grain boundary phase, thereby improving flexural strength at both room and elevated temperatures [33,34]. Notably, we introduced a novel component combination designed to form a high-entropy grain boundary phase. High-entropy systems, known for their high configurational entropy and compositional complexity, have shown enhanced performance in various applications, such as wave-absorbing materials, energy storage systems, composites, and thermal management materials [35–39]. Extending this entropy engineering strategy to ceramic systems offers great potential for enhancing the mechanical properties of Si_3N_4 ceramics. Building on this approach, the use of multiple RE_2O_3 additives not only regulates grain growth in the liquid phase during sintering but also promotes the formation of a high-entropy grain boundary phase during cooling. This dual strategy enables synergistic optimization of both flexural strength and fracture toughness through tailored microstructure and grain boundary engineering.

This study pioneers the application of high-entropy engineering to Si_3N_4 ceramics. We incorporate five RE_2O_3 with SiO_2 as sintering additives to fabricate Si_3N_4 ceramics via hot pressing sintering (HPS). We systematically investigate how the multicomponent RE-ion liquid phase governs phase transformation, densification, and microstructural evolution. Furthermore, we explore the crystallization of the liquid phase into high-entropy $RE_2Si_2O_7$ and its impact on the mechanical properties. A comparative analysis with single RE_2O_3 additives confirms the superiority of this high entropy approach, establishing a new paradigm for optimizing liquid phase sintered ceramics through entropy-driven design.

2 Experimental

2.1 Raw materials and formulation

The starting materials consisted of high-purity α-Si_3N_4 powder (SN-E10, α-phase content > 95%) with five RE_2O_3 (Gd_2O_3, Y_2O_3, Yb_2O_3, Lu_2O_3, and Sc_2O_3; purity > 99.99% each) and SiO_2 (purity > 99.99%). The sintering additives RE_2O_3 and SiO_2 were formulated with a stoichiometric ratio according to $RE_2Si_2O_7$, where the five RE elements maintained equimolar proportions (Gd : Y : Yb : Lu : Sc = 1 : 1 : 1 : 1 : 1). This formulation enabled the *in situ* formation of high-entropy $RE_2Si_2O_7$ at the grain boundary phase of Si_3N_4 ceramics. The molar ratio of α-Si_3N_4 to multiple additives was varied as 94 : 6, which was labeled $5RE_{0.2}$-SN. Additional compositions with 20 and 50 mol% additives were prepared to enhance the high-entropy grain boundary phase content. Control groups were established using unitary RE_2O_3 + SiO_2 additives (RE = Gd, Y, Yb, Lu, and Sc), each containing 6 mol% additives, which were labeled Gd-SN, Y-SN, Yb-SN, Lu-SN, and Sc-SN, respectively.

2.2 Preparation of Si_3N_4 ceramics

The fabrication process combined wet milling and HPS. The additive mixtures and α-Si_3N_4 powder were added in two stages to anhydrous ethanol for homogenization via planetary ball milling (350 r/min, 10 h) within a nylon container. The milling was conducted with a ball-to-powder ratio of 2 : 1, employing 5 and 10 mm Si_3N_4 grinding media at a 1 : 1 mass ratio. The resultant slurry was dried, sieved, and uniaxially pressed at 10 MPa to form green bodies. Subsequent sintering was conducted in a graphite die under biaxial mechanical pressure (30 MPa) with a nitrogen atmosphere (0.1 MPa). A sintering temperature of 1750 °C was implemented, with a holding time of 2 h. The main synthesis route for Si_3N_4 ceramics with a high-entropy grain boundary phase is illustrated in Fig. 1.

2.3 Characterizations

The shrinkage behavior was measured using in situ shrinkage curves in an HPS furnace (ZT-100-18Y, Shanghai Chenhua Science Technology Co., Ltd., China) with minimal mechanical pressure (3 MPa) applied. Bulk densities were determined by Archimedes' method with theoretical densities calculated through the rule of mixtures. Flexural strength was evaluated via three-point bending tests (specimen dimensions: 3 mm × 4 mm × 36 mm, span: 30 mm) on a universal testing machine (LD23.104, LSI, China) with a loading rate of 0.5 mm/s, reporting an average of ≥ 5 valid measurements. Fracture toughness was assessed using the single-edge notched beam method (specimen dimensions: 3 mm × 4 mm × 20 mm with 2 mm notch depth and 0.2 mm notch width, span: 16 mm) under a loading rate of 0.05 mm/s, averaging ≥ 5 successful tests. Phase composition analysis was performed using a Cu Kα X-ray diffractometer (XRD; Shimadzu 6100, Shimadzu, Japan) with Rietveld refinement implemented in GSAS software. The polished surface of Si_3N_4 ceramics was etched using CF_4 at 50 W for 600 s. Microstructural characterization employed a field-emission scanning electron microscope (FE-SEM; Regulus 8100, Hitachi, Japan), a field-emission transmission electron microscopy (FE-TEM; Talos F200X, FEI, USA), and TEM-coupled energy-dispersive X-ray spectroscope (EDS). All characterizations were conducted at ambient temperature. The scanning electron microscopy (SEM) images were identified by commercial software (MIPAR) and analyzed for microstructural parameters.

3 Results and discussion

3.1 Composition and structure analysis of the grain boundary phase in Si_3N_4 ceramics

Based on the effects of different RE^{3+} on the grain growth of Si_3N_4

ceramics and the design guidelines of $RE_2Si_2O_7$, we selected five RE elements (Gd, Y, Yb, Lu, and Sc) that are often used as sintering additives for Si_3N_4 ceramics with different ionic radii and moderate average ionic radius differences. Si_3N_4 ceramics with a high-entropy grain boundary phase were designed and prepared by utilizing the synergistic effect of multiple RE_2O_3 as sintering additives on Si_3N_4 grain growth. To systematically investigate the entropy engineering effects on microstructural evolution, particularly grain boundary phase formation, we fabricated Si_3N_4 ceramics with multiple RE_2O_3 as sintering additives at varying content levels (6, 20, and 50 mol%). Figure 2(a) presents the XRD patterns elucidating phase evolution with increasing additive content. All specimens exhibited a dual-phase constitution consisting of a β-Si_3N_4 phase (PDF#09-0259) and a β-$(Gd_{0.2}Y_{0.2}Yb_{0.2}Lu_{0.2}Sc_{0.2})_2Si_2O_7$ grain boundary phase (PDF#22-1103). The characteristic peaks of β-$(Gd_{0.2}Y_{0.2}Yb_{0.2}Lu_{0.2}Sc_{0.2})_2Si_2O_7$ differ from the diffraction patterns of $Sc_2Si_2O_7$, $Y_2Si_2O_7$, and $Gd_2Si_2O_7$ [40], indicating the formation of a solid solution comprising all five RE elements. Notably, the characteristic diffraction peaks corresponding to β-$(Gd_{0.2}Y_{0.2}Yb_{0.2}Lu_{0.2}Sc_{0.2})_2Si_2O_7$ displayed intensity dependence on additive concentration. At low additive loading (6 mol%), the $RE_2Si_2O_7$ phase signatures remained relatively weak due to the limited phase fraction. Progressive peak intensification observed at 20 and 50 mol% additives confirmed enhanced grain boundary phase formation in Si_3N_4 ceramics. The Rietveld refinement results in Fig. 2(b) demonstrate excellent agreement between the experimental and simulated patterns. The refinement quality parameters (Chi-square $X^2 = 1.822$; weighted profile factor, $R_{wp} < 10\%$) validate the accuracy of phase quantification, with determined phase ratios matching the designed compositional specifications.

To elucidate the grain boundary phase structure in Si_3N_4 ceramics, high-resolution transmission electron microscopy (HRTEM) analysis was performed, as depicted in Fig. 3(b). The HRTEM image distinctly reveals two sets of lattice fringes with measured spacings of 0.668 and 0.467 nm, corresponding to the (100) plane of β-Si_3N_4 and (001) plane of high-entropy β-$(Gd_{0.2}Y_{0.2}Yb_{0.2}Lu_{0.2}Sc_{0.2})_2Si_2O_7$, respectively. The complementary TEM-EDS elemental mappings in Figs. 3(c) and 3(d) demonstrate homogeneous elemental dispersion of Si, N, Gd, Y, Yb, Lu, and Sc across the nanoscale domains, confirming the successful formation of well-crystallized and chemically uniform high-entropy $(Gd_{0.2}Y_{0.2}Yb_{0.2}Lu_{0.2}Sc_{0.2})_2Si_2O_7$ phases at the grain boundary phase in Si_3N_4 ceramics. In contrast, the Y-SN control sample exhibits a poorly crystalline grain boundary phase with substantial amorphous content, showing significantly lower

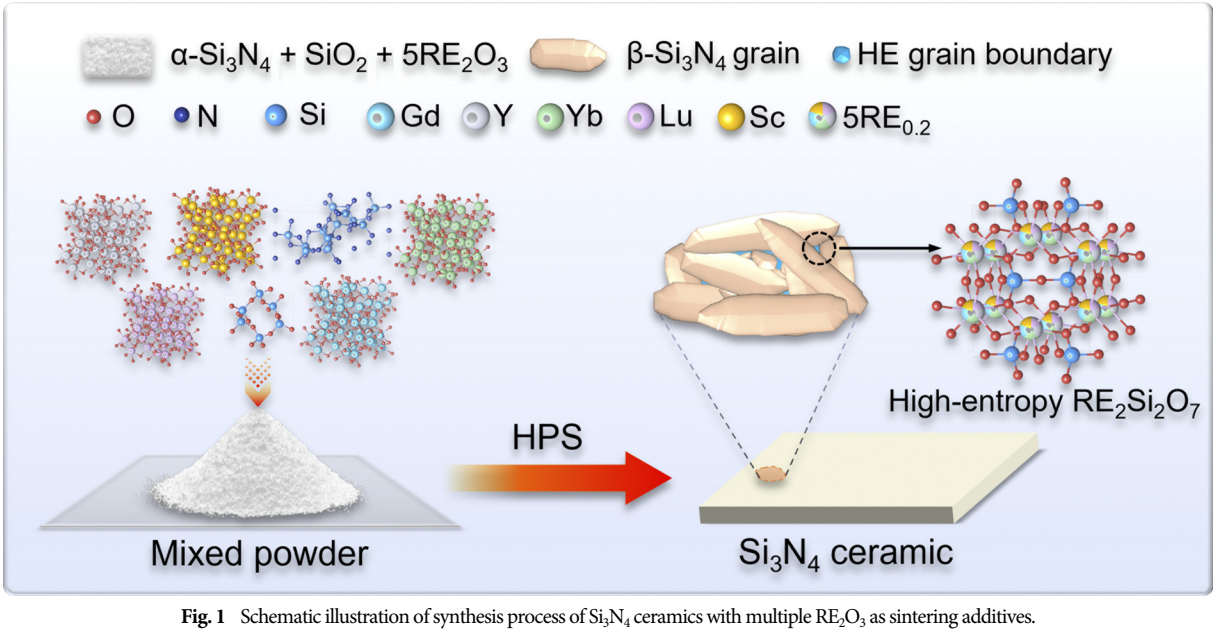

Fig. 1 Schematic illustration of synthesis process of Si_3N_4 ceramics with multiple RE_2O_3 as sintering additives.

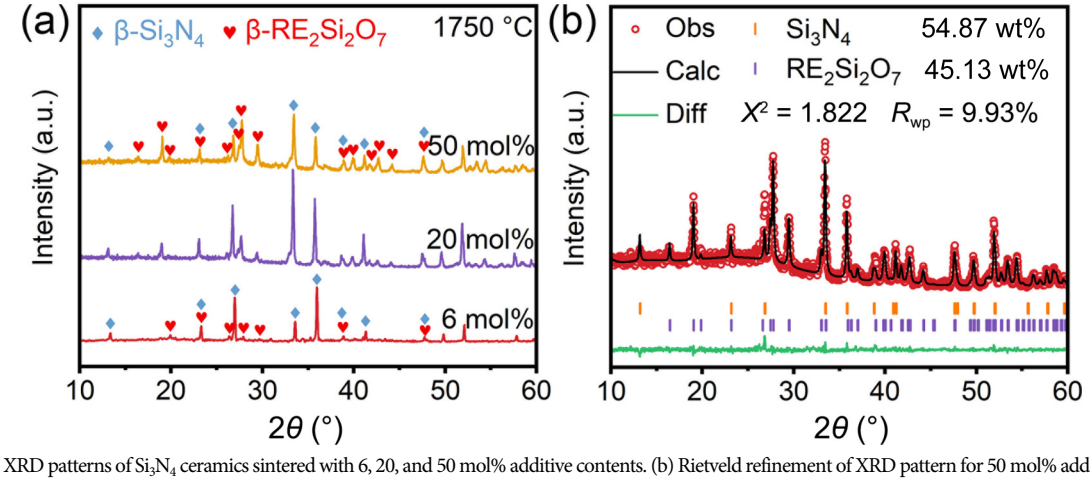

Fig. 2 (a) XRD patterns of Si_3N_4 ceramics sintered with 6, 20, and 50 mol% additive contents. (b) Rietveld refinement of XRD pattern for 50 mol% additive sample.

清华大学出版社 Tsinghua University Press | SciOpen

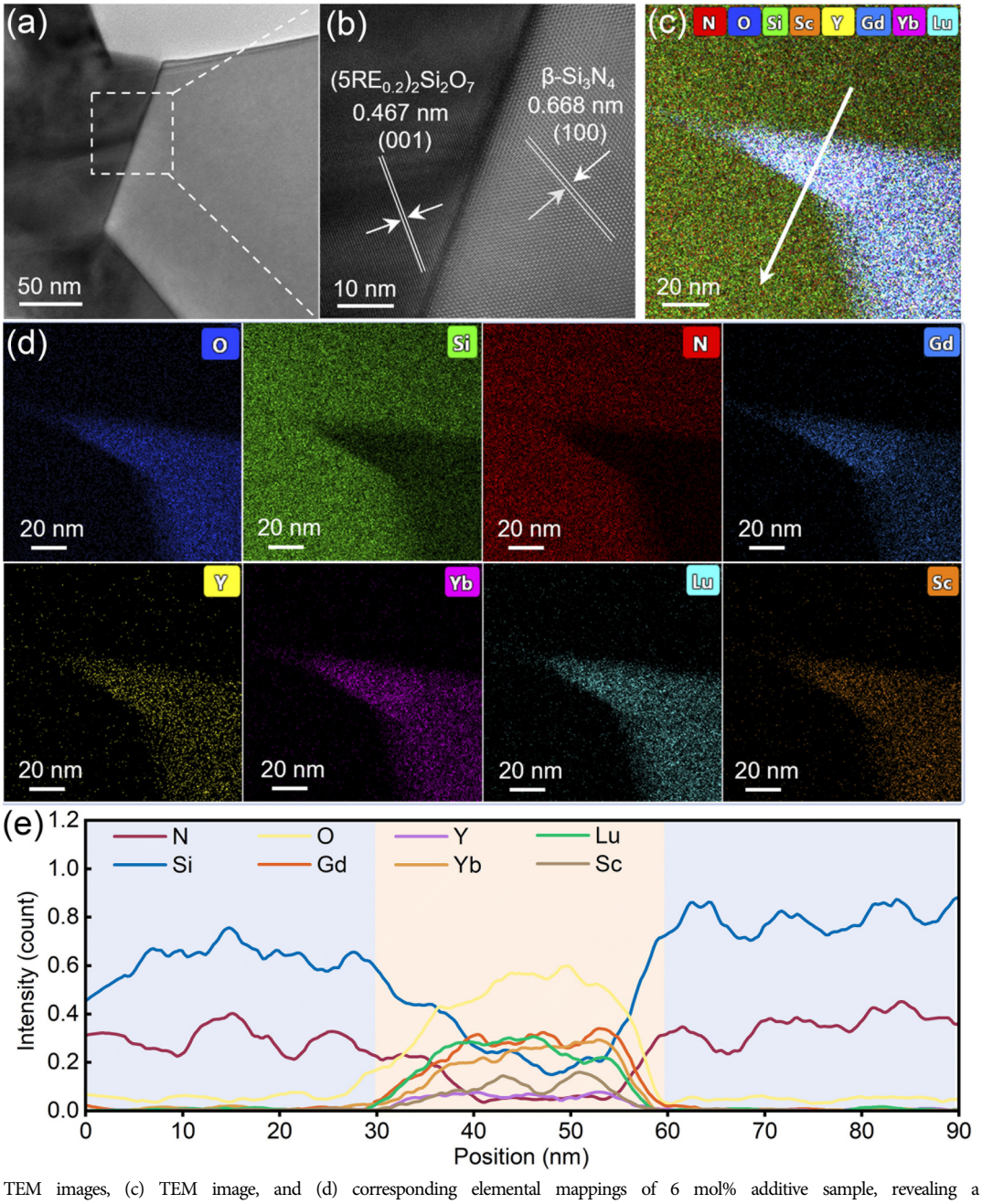

Fig. 3 (a, b) TEM images, (c) TEM image, and (d) corresponding elemental mappings of 6 mol% additive sample, revealing a high-entropy $(Gd_{0.2}Y_{0.2}Yb_{0.2}Lu_{0.2}Sc_{0.2})_2Si_2O_7$ grain boundary phase. (e) EDS line scan element distribution profile along white arrow in (c).

crystallinity than the $5RE_{0.2}$-SN sample, as evidenced by the TEM data in Fig. S1 in the Electronic Supplementary Material (ESM). In Fig. 3(e), the EDS spectral lines presented along the white arrows show the elemental content in each region, further confirming the homogeneity within each region. In addition, EDS analysis also verified that the proportions of these elements conformed to the design ratios (Table 1). The above experiments demonstrate the controlled *in situ* precipitation of highly crystalline high-entropy $(Gd_{0.2}Y_{0.2}Yb_{0.2}Lu_{0.2}Sc_{0.2})_2Si_2O_7$ at the grain boundary phase in Si_3N_4 ceramics using multiple RE_2O_3 as sintering additives.

Table 1 TEM-EDS analysis results of 6 mol% additive sample in Fig. 3(c)

Element	Family	Atomic fraction (%)	Atomic error (%)
N	K	46.03	6.48
O	K	16.08	3.91
Si	K	33.98	8.05
Sc	K	0.70	0.13
Y	K	0.97	0.18
Gd	L	0.71	0.12
Yb	L	0.74	0.13
Lu	L	0.79	0.14

3.2 Liquid phase regulation of multiple RE_2O_3 as sintering additives on the microstructure evolution in Si_3N_4 ceramics

To assess the significant effects of multiple RE_2O_3 as sintering additives on liquid phase regulation, five control Si_3N_4 ceramics were prepared, each containing a single RE^{3+} additive (6 mol%, RE = Gd, Y, Yb, Lu, and Sc). As shown in Fig. 4(a), the *in situ* displacement speed curves at a constant pressure of 3 MPa during sintering show the shrinkage behavior of the six Si_3N_4 ceramics.

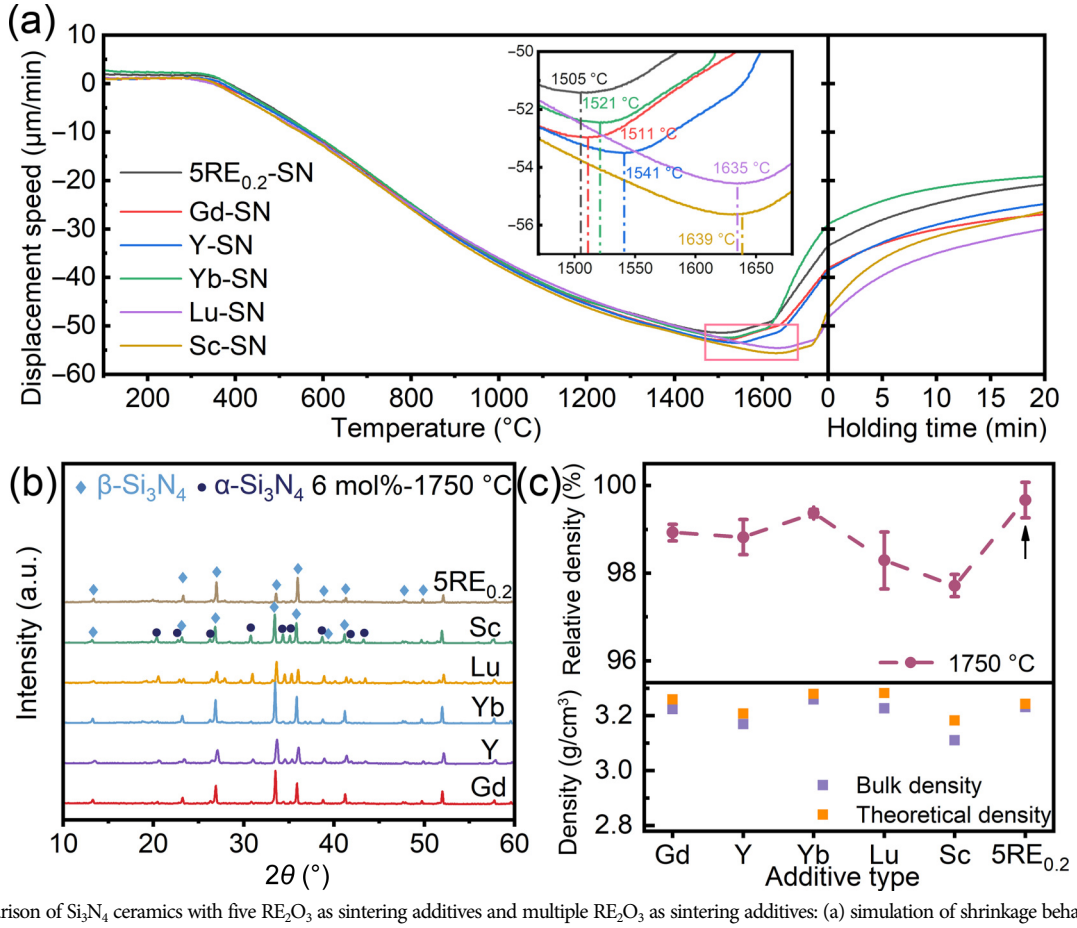

Fig. 4 Comparison of Si_3N_4 ceramics with five RE_2O_3 as sintering additives and multiple RE_2O_3 as sintering additives: (a) simulation of shrinkage behaviors (constant pressure = 3 MPa), (b) XRD patterns, and (c) relative density, bulk density, and theoretical density.

Due to the relatively high eutectic points of the Lu_2O_3–SiO_2 and Sc_2O_3–SiO_2 systems, the onset temperature of shrinkage for these two additive systems in Si_3N_4 ceramics is also relatively high (exceeding 1600 °C) [41–45]. Interestingly, based on the eutectic effect of multiple RE_2O_3 as sintering additives, its onset temperature of shrinkage (approximately 1503 °C) is lower than that of the other five unitary RE_2O_3 as sintering additives, allowing for an earlier onset temperature of shrinkage. The configurational entropy increase resulting from the multicomponent RE-ion liquid phase design generated a high-entropy effect that enhanced the solid solution process of the multiple RE_2O_3 [46]. Additionally, we individually prepared high-entropy $RE_2Si_2O_7$ and five unitary $RE_2Si_2O_7$ phases in a muffle furnace. As shown in Fig. S2 in the ESM, the XRD results indicate that when the sintering temperature exceeds 1600 °C, the five unitary $RE_2Si_2O_7$ compounds form different crystalline phases due to differences in RE^{3+} radii, including α-$Gd_2Si_2O_7$, γ-$Y_2Si_2O_7$, β-$Yb_2Si_2O_7$, β-$Lu_2Si_2O_7$, and β-$Sc_2Si_2O_7$. In this study, by controlling the average ionic radius of the selected rare earth elements below 0.885 Å, a quinary high-entropy phase consisting of β-$(Gd_{0.2}Y_{0.2}Yb_{0.2}Lu_{0.2}Sc_{0.2})_2Si_2O_7$ was successfully synthesized. This demonstrates that the resulting grain boundary phase is a single-phase solid solution rather than a mixture of multiple $RE_2Si_2O_7$ phases. From the perspective of phase purity, even at 1650 °C, $Sc_2Si_2O_7$ struggles to form a pure single-phase solid solution, whereas the high-entropy system successfully achieves a homogeneous single-phase solid solution. These results fully demonstrate that the high-entropy effect in this system effectively promotes the crystallization of the grain boundary phase into single-phase $(Gd_{0.2}Y_{0.2}Yb_{0.2}Lu_{0.2}Sc_{0.2})_2Si_2O_7$. Therefore, we infer that the initial liquid phase formation temperature for multiple RE_2O_3 as sintering additives should be lower than that for five unitary RE_2O_3 as sintering additives.

Simultaneously, variations in the RE-ion radius (r^{3+}) alter the ionic field strength, which in turn affects the liquid phase properties. Specifically, RE ions with smaller radii possess a stronger RE ion field strength, which results in higher viscosity. At lower sintering temperatures, the less viscous liquid phase facilitates the dissolution and precipitation of Si_3N_4 grains, leading to greater shrinkage. Achieving significant shrinkage with a more viscous liquid phase requires a relatively high sintering temperature. This higher viscosity hinders grain growth and densification in Si_3N_4 ceramics. In this work, $r(Gd^{3+}) > r(Y^{3+}) > r(Yb^{3+}) > \bar{r}(5RE_{0.2}{}^{3+}) > r(Lu^{3+}) > r(Sc^{3+})$. Lu-SN and Sc-SN specimens exhibit higher liquid viscosity than $5RE_{0.2}$-SN, Gd-SN, Y-SN, and Yb-SN. This elevated viscosity restricts α→β phase transformation and limits grain growth in Lu-doped or Sc-doped ceramics, as shown in Figs. 4(b) and 4(c) and Table S1 and S2 in the ESM, resulting in insufficient grain growth and incomplete densification with residual hole defects. In contrast, $5RE_{0.2}$-SN has a relatively complete phase transition and densification despite a moderate average $5RE_{0.2}{}^{3+}$ radius combined with a low onset temperature of shrinkage.

Larger-radius RE^{3+} ions (such as Gd^{3+}, Y^{3+}, and Yb^{3+}) preferentially adsorb on prismatic Si_3N_4 surfaces, suppressing SiN adsorption and promoting axial grain growth (high aspect ratios). Conversely, smaller RE^{3+} ions (such as Lu^{3+} and Sc^{3+}) enhance radial growth, producing larger diameter grains with lower aspect ratios [17]. From the fracture surfaces SEM of Si_3N_4 ceramics in Fig. 5, it is observed that the grain growth of $5RE_{0.2}$-SN, Gd-SN,

Y-SN, and Yb-SN is more significant than that of Lu-SN and Sc-SN. This further validates that the differences in RE-ion adsorption on the β-Si_3N_4 prismatic planes within the liquid phase affect the microstructure of Si_3N_4 ceramics. The significant grain development observed in $5RE_{0.2}$-SN is inferred to result from the synergistic effect of the five RE ions, which is similar to the binary system reported by Lu *et al.* [47]. All of the above results verified that multiple RE_2O_3 as sintering additives significantly optimized the phase transition, grain growth, and densification of Si_3N_4 grains by modulating the liquid phase properties.

3.3 Synergistic optimization and mechanism analysis of mechanical properties in Si_3N_4 ceramics

Based on the differences in the nature of the liquid phase produced by different RE elements and the different modulation effects of the RE element species on the Si_3N_4 grains, we further evaluated the mechanical properties of Si_3N_4 ceramics prepared by different RE_2O_3 as sintering additives. Among the five unitary additive systems, the Lu-SN and Sc-SN samples showed poor mechanical strength less than 1000 MPa and toughness less than 8.4 MPa·m$^{1/2}$), as shown in Fig. 6. The good mechanical properties

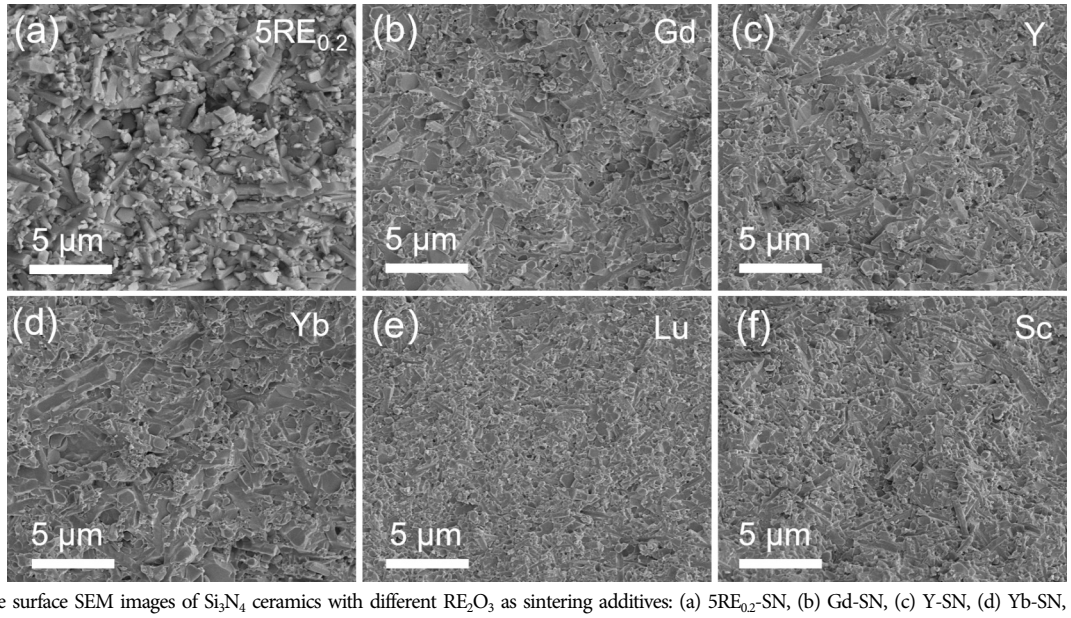

Fig. 5 Fracture surface SEM images of Si_3N_4 ceramics with different RE_2O_3 as sintering additives: (a) $5RE_{0.2}$-SN, (b) Gd-SN, (c) Y-SN, (d) Yb-SN, (e) Lu-SN, and (f) Sc-SN.

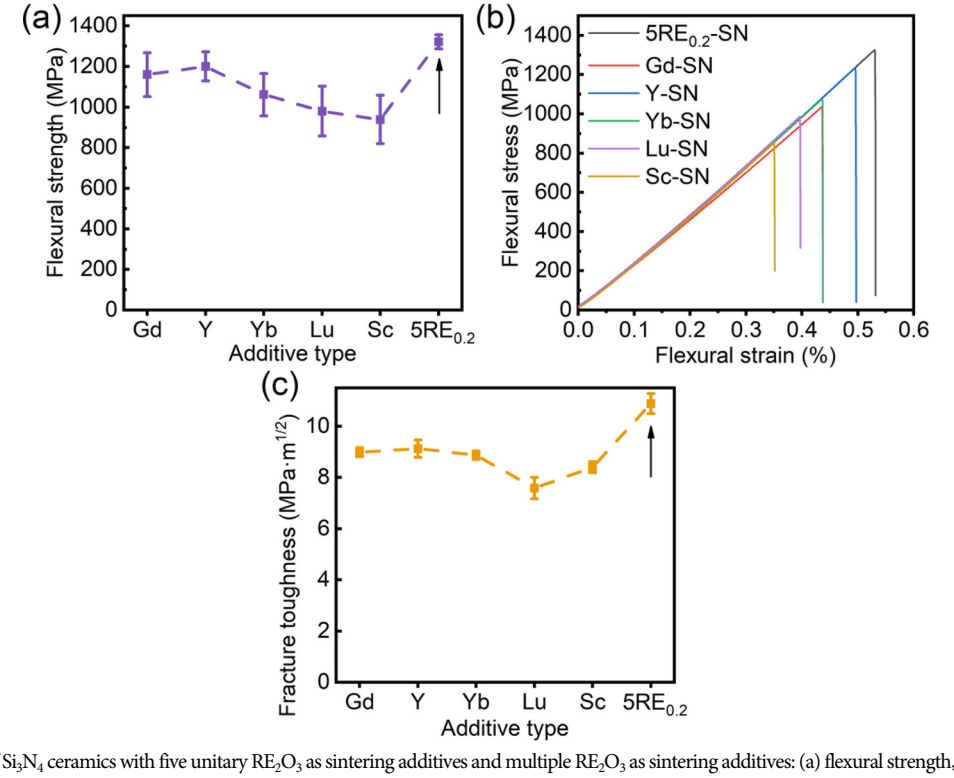

Fig. 6 Comparison of Si_3N_4 ceramics with five unitary RE_2O_3 as sintering additives and multiple RE_2O_3 as sintering additives: (a) flexural strength, (b) stress–strain curve, and (c) fracture toughness.

of the Gd-SN, Y-SN, and Yb-SN samples stem from their well-developed grain morphology (balanced aspect ratios) and complete densification, which contrasts with the defective microstructures of the Lu-SN and Sc-SN samples.

Notably, $5RE_{0.2}$-SN exhibited excellent flexural strength and fracture toughness, of 1322±34 MPa and 10.88±0.39 MPa·$m^{1/2}$, respectively, which showed mechanical properties superior to those of the five unitary RE additive systems. The flexural strength and fracture toughness of 5RE0.2-SN were significantly higher than those of the unitary additive system. Relative to the average flexural strength (1068 MPa) and fracture toughness (8.59 MPa·$m^{1/2}$) of the five unitary RE additive systems, $5RE_{0.2}$-SN exhibited improvements of 23.78% and 26.65%, respectively. Meanwhile, the fracture strain of $5RE_{0.2}$-SN was at a higher level (0.53%) than that of the five unitary additive systems. It is obvious that the flexural strength and fracture toughness can be synergistically improved by this synergistic action of the multicomponent RE-ion liquid phase.

The mechanical properties of Si_3N_4 ceramics are closely related to their microscopic morphology. Smaller grains are favorable for the strengthening of Si_3N_4 ceramics, while rod-like β-Si_3N_4 grains with high aspect ratios can toughen Si_3N_4 ceramics by grain pull-out and crack deflection. To further analyze the mechanism of this size effect on the mechanical properties of Si_3N_4 ceramics, we performed image analysis on the surface SEM of $5RE_{0.2}$-SN after etching, together with a comparison analysis of Y-SN, which has better mechanical properties among the five unitary RE_2O_3 as sintering additives. As shown in Fig. 7, $5RE_{0.2}$-SN exhibits a greater number and larger size of rod-like β-Si_3N_4 grains than Y-SN at the same magnification. Based on the corresponding grain size distribution diagram (Fig. 8(c)), it can be observed that in the Y-SN sample, grains with diameters exceeding 0.750 μm accounted for merely 0.53%, while those with diameters smaller than 0.120 μm constituted 35.86%. Additionally, 50% of the grains exhibited diameters greater than 0.153 μm. Under the effect of multiple RE_2O_3 as sintering additives, grain diameters larger than 0.750 μm in the $5RE_{0.2}$-SN sample increased significantly to 3.24%, with smaller grains (d < 0.120 μm) accounting for 36.44% (Fig. 8(a)). Moreover, 50% of the grains exhibited diameters less than or equal to 0.145 μm. Building upon the aforementioned grain size statistics, we calculated their aspect ratios and found that in $5RE_{0.2}$-SN, grains with aspect ratios (l/d) greater than 4 accounted for 3.42%, while over 50% of grains possessed aspect ratios greater than 1.78 (Fig. 8(b)). In contrast, the Y-SN sample contained only 0.77% grains with aspect ratios exceeding 4, and its median aspect ratio was more than 1.61 (Fig. 8(d)).

Integrating the grain size distribution and aspect ratio statistics, the $5RE_{0.2}$-SN sample exhibits a higher proportion of fine grains and rod-like β-Si_3N_4 grains with elevated aspect ratios, demonstrating a characteristic bimodal microstructure. According to the Hall–Petch equation (Eq. (1)) [48]:

$$\sigma = \sigma_0 + kd^{-1/2} \tag{1}$$

where σ represents the actual strength of the material, σ_0 and k are material constants, and d is the average grain size. The high proportion of fine grains in the $5RE_{0.2}$-SN sample contributed to its excellent flexural strength. Si_3N_4 ceramics are composed of Si_3N_4 grains and a grain boundary phase. In addition to the influence of grain size on flexural strength, the strength of the grain boundary phase also affects the overall strength of the ceramic, with a higher grain boundary phase strength leading to a higher ceramic strength. The grain boundary phases in the five unitary RE_2O_3 samples as sintering additives are predominantly amorphous. However, the design of novel multiple RE_2O_3 as sintering additives strategically harnesses synergistic interactions among multicomponent RE-ion liquid phases to regulate grain morphology and establish distinct bimodal microstructures while simultaneously enabling the designed liquid phase to react with silica during cooling, which precipitates a well-crystallized high-entropy grain boundary phase upon sintering completion benefiting from the high-entropy effect [33,34]. The strength of this crystalline high-entropy grain boundary phase is higher than

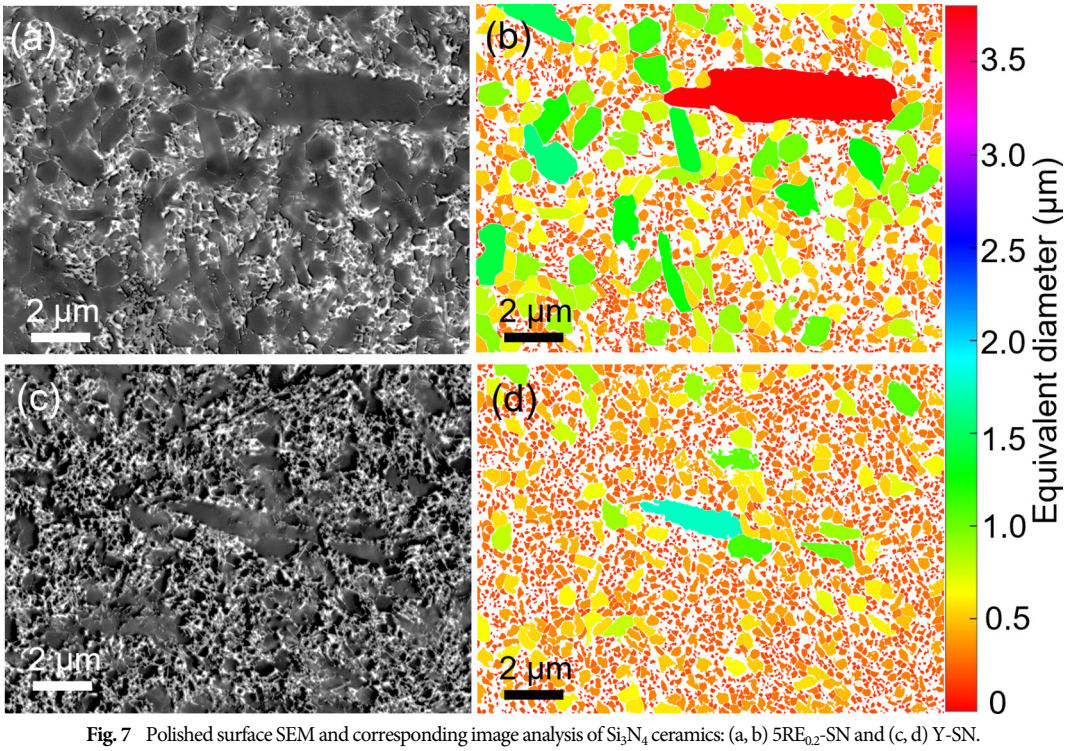

Fig. 7 Polished surface SEM and corresponding image analysis of Si_3N_4 ceramics: (a, b) $5RE_{0.2}$-SN and (c, d) Y-SN.

that of the grain boundary glassy phase. Therefore, the high-entropy $(Gd_{0.2}Y_{0.2}Yb_{0.2}Lu_{0.2}Sc_{0.2})_2Si_2O_7$ grain boundary phase in $5RE_{0.2}$-SN also plays a critical role in enhancing the overall strength of Si_3N_4 ceramics.

In addition, elongated rod-like β-Si_3N_4 grains contribute to toughening but cannot fully ensure that the Si_3N_4 ceramics achieve a toughening effect [49,50]. Toughening processes such as crack bridging or crack deflection only occur when a crack propagates along the prismatic planes of these elongated β-Si_3N_4 grains. Therefore, an appropriately weakened grain boundary structure is essential. When the thermal expansion coefficient of the grain boundary phase is greater than that of the Si_3N_4 matrix, it generates interfacial tensile stress at the Si_3N_4 grain/grain boundary phase interface [31,32]. This stress can appropriately enhance the fracture toughness of Si_3N_4 ceramics. Additionally, the sintering additives form a highly crystalline high-entropy grain boundary phase after liquid-phase cooling in Si_3N_4 ceramics. The thermal expansion coefficient of the grain boundary phase remains higher than that of the grain boundary glassy phase. This thermal expansion mismatch generates residual tensile stress at the Si_3N_4 grain/grain boundary phase interfaces. The introduction of high-entropy grain boundary phases promotes interface debonding, shifting the fracture mode in Si_3N_4 ceramics from transgranular to intergranular. This transition enhances the fracture toughness of Si_3N_4 ceramics [51]. The synergistic interaction between a high proportion of elongated Si_3N_4 grains and a highly crystalline high-entropy grain boundary phase with optimized thermal expansion matching facilitates the transition from transgranular to intergranular fracture in Si_3N_4 ceramics. As seen in Fig. 9, this significantly achieves self-toughening of the Si_3N_4 ceramics through mechanisms such as crack deflection, crack bridging, and grain pull-out.

Subsequently, we compared the mechanical properties of Si_3N_4 ceramics prepared by different sintering methods in previous work (Fig. 10). The corresponding mechanical property testing methods are shown in Table 2. Under HPS technology, the advantages conferred by our design of the additive composition are highly significant. $5RE_{0.2}$-SN exhibits superior mechanical properties relative to HPS Si_3N_4 ceramics with conventional additives such as RE_2O_3+MgO [30], RE_2O_3+Al_2O_3 [51–53], and RE_2O_3+Si_3N_4 seeds [54,55]. This performance enhancement results from the control of grain growth by the multicomponent RE-ion liquid phase, which is synergistically integrated with the designed crystallization of the high-entropy grain boundary phase. This approach achieves the highest reported values of both flexural strength and fracture toughness by HPS lighting. These results indicate that the highly crystalline high-entropy $(Gd_{0.2}Y_{0.2}Yb_{0.2}Lu_{0.2}Sc_{0.2})_2Si_2O_7$ grain boundary phase, coupled with

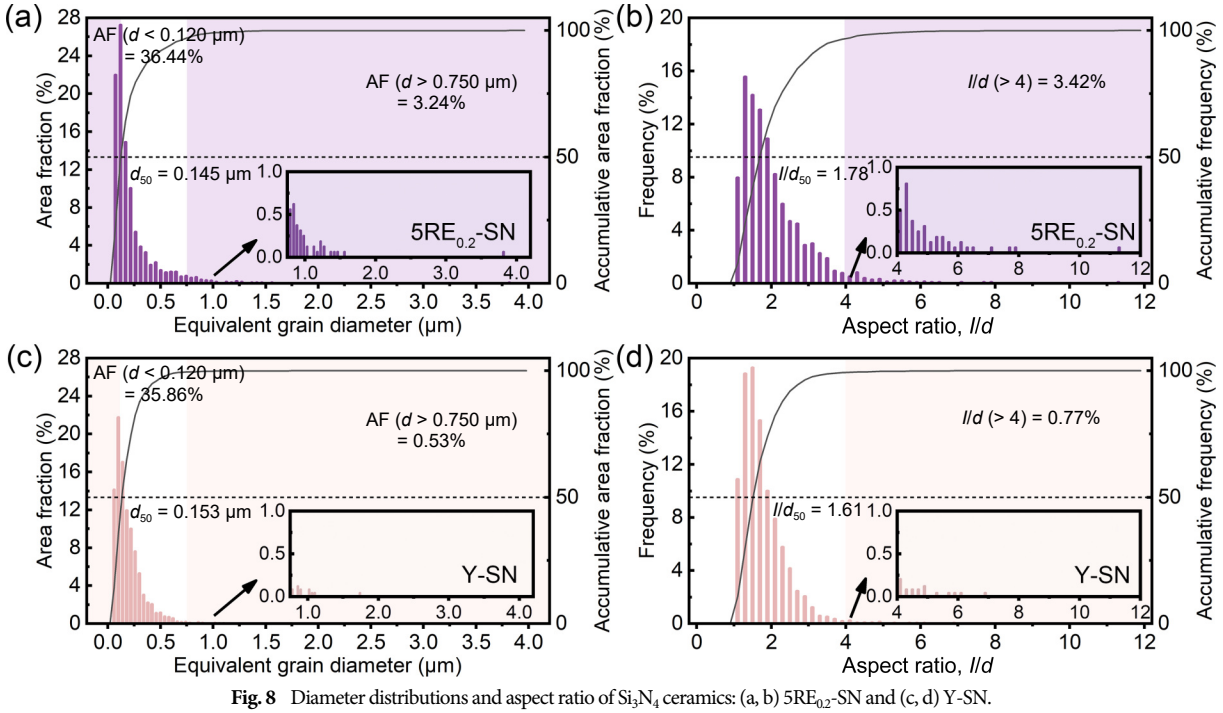

Fig. 8 Diameter distributions and aspect ratio of Si_3N_4 ceramics: (a, b) $5RE_{0.2}$-SN and (c, d) Y-SN.

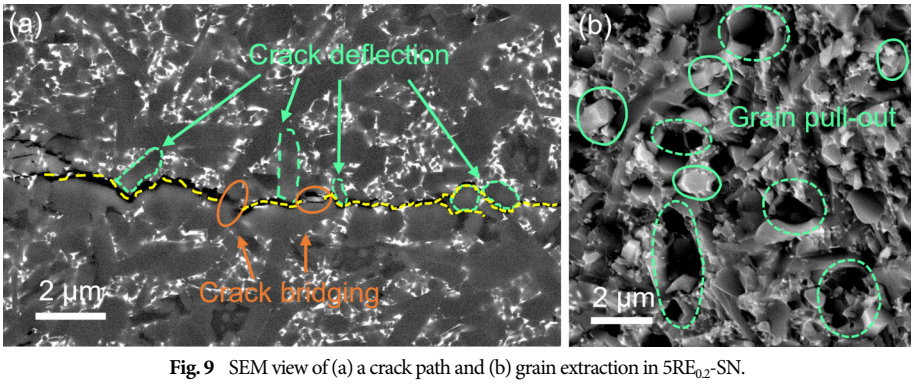

Fig. 9 SEM view of (a) a crack path and (b) grain extraction in $5RE_{0.2}$-SN.

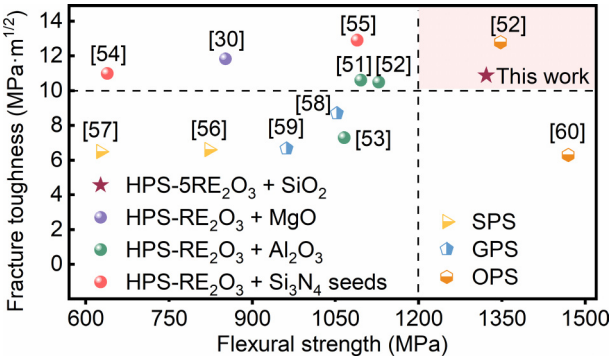

Fig. 10 Comparison of flexural strength and fracture toughness of $5RE_{0.2}$-SN material obtained in this study with previously reported data for Si_3N_4 ceramics fabricated by different sintering methods.

its interlocking distribution with the two distinct grain types, contributes to both grain refinement strengthening and self-toughening via elongated grains. This synergy leads to the simultaneous optimization of flexural strength and fracture toughness in $5RE_{0.2}$-SN.

Beyond HPS, we also compared our work with Si_3N_4 ceramics prepared by spark plasma sintering (SPS), gas pressure sintering (GPS), and oscillatory pressure sintering (OPS). SPS is characterized by rapid heating and cooling rates. Due to its short holding time and lower sintering temperature, the resulting Si_3N_4 ceramics exhibit fine grains. Grain refinement strengthening contributes to their relatively high flexural strength, although it remains lower than that of the $5RE_{0.2}$-SN sample in this work. Concurrently, their smaller size and lower aspect ratio of rod-like β-Si_3N_4 grains result in inferior fracture toughness [56,57]. GPS allows for sufficient grain growth in Si_3N_4 ceramics, resulting in prominent elongated rod-like β-Si_3N_4 grains. Despite achieving higher fracture toughness at the expense of a slight flexural strength reduction, both mechanical properties of Si_3N_4 ceramics by GPS remain below those of our $5RE_{0.2}$-SN sample [58,59]. Interestingly, the hot-forging process utilized in OPS prepared Si_3N_4 ceramics with elongated finer grains, higher density, and fewer grain boundary defects. In particular, the presence of abundant Moiré' patterns at the grain boundary indicates that Si_3N_4 grains slide and rotate, achieving optimal alignment. This results in exceptional flexural strength and fracture toughness [52,60]. In this work, optimization of the additive composition alone achieved comprehensive mechanical properties comparable to those of OPS-processed ceramics. Our material design strategy incorporating multiple RE_2O_3 as sintering additives and a high-entropy grain boundary phase provides significant advantages for enhancing the mechanical properties of Si_3N_4 ceramics. Synergistic integration of this approach with OPS processing benefits holds promising potential for developing Si_3N_4 ceramics with exceptional mechanical properties.

Table 2 Testing methods for mechanical properties of different Si_3N_4 ceramics in Fig. 10

Sintering methods	Flexural strength (MPa)	Testing method	Fracture toughness (MPa·m$^{1/2}$)	Testing method	Ref.
HPS	852	Four-point bending	11.84	Single-edge notched beam (three-point bending)	[30]
HPS	1096	Three-point bending	10.61	Vickers indentation method	[51]
HPS	1128	Three-point bending	10.50	Single-edge notched beam	[52]
HPS	1066	Three-point bending	7.30	Vickers indentation method	[53]
HPS	639	Four-point bending	11.00	Single-edge precracked beam	[54]
HPS	1089	Three-point bending	12.90	Single-edge notched beam	[55]
SPS	822	Three-point bending	6.60	Single-edge notched beam	[56]
SPS	627	Three-point bending	6.50	Vickers indentation method	[57]
GPS	1053	Three-point bending	8.70	Single-edge precracked beam	[58]
GPS	962	Three-point bending	6.67	Vickers indentation method	[59]
OPS	1470	Three-point bending	6.30	Vickers indentation method	[60]
OPS	1348	Three-point bending	12.80	Single-edge notched beam	[52]
HPS	1322	Three-point bending	10.88	Single-edge notched beam	This work

4 Conclusions

In summary, synergistic optimization of flexural strength and fracture toughness in Si_3N_4 ceramics was achieved via a high-entropy strategy. The multicomponent RE-ion liquid phase, derived from multiple RE_2O_3 as sintering additives, reduces the shrinkage onset temperature while accelerating α → β phase transformation and densification. Low viscosity and multicomponent RE-ion interactions in this liquid phase facilitate anisotropic growth of Si_3N_4 grains, forming a bimodal microstructure with high aspect ratio rod-like β-Si_3N_4 grains embedded in a fine-grained matrix. Moreover, the enhanced crystallinity of this phase generates a high-strength crystalline $(Gd_{0.2}Y_{0.2}Yb_{0.2}Lu_{0.2}Sc_{0.2})_2Si_2O_7$ grain boundary phase (replacing glassy phases), elevating the mechanical strength. Concurrently, its higher thermal expansion coefficient versus glassy phases induces interfacial tensile stress that actively drives crack deflection. Integration of this tailored bimodal structure and high-entropy grain boundary phase delivers exceptional mechanical properties: 1322 MPa flexural strength and 10.88 MPa·m$^{1/2}$ fracture toughness. The $5RE_{0.2}$-SN sample outperforms all unitary RE_2O_3 as sintering additive counterparts by 23.78% in strength and 26.65% in toughness versus average, confirming the exceptional potential of Si_3N_4 ceramics featuring a high-entropy grain boundary phase for structural applications. This work establishes high-entropy engineering as a novel pathway for performance optimization in Si_3N_4 ceramics. The extensible grain boundary design paradigm demonstrated herein will stimulate transformative innovation across liquid phase sintered ceramic technologies.

Acknowledgements

This work was financially supported by the National Natural Science Foundation of China, Young Program (No. 52202077), the Hunan Provincial Natural Science Foundation of China, General Program (No. 2024JJ5407), the Science Foundation of the

National Key Laboratory of Science and Technology on Thermostructural Composite Materials (No. 2022-JCJQ-LB-073), the Science Foundation of National Key Laboratory of Science and Technology on Advanced Composites in Special Environments (No. JCKYS2024603C010), and the Hunan Province Postgraduate Research and Innovation Project (No. CX20240122).

Availability of data and materials

The data that support the findings of this study are available from the corresponding author upon reasonable request.

Competing interests

The authors have no competing interests to declare that are relevant to the content of this article.

Electronic Supplementary Material

Supplementary material is available in the online version of this article at https://doi.org/10.26599/JAC.2025.9221230.

References

[1] Tang SJ, Guo WM, Sun SK, *et al.* Design strategy of phase and microstructure of Si_3N_4 ceramics with simultaneously high hardness and toughness. *J Adv Ceram* 2023, **12**: 122–131.

[2] Zhang J, Liu GH, Cui W, *et al.* Plastic deformation in silicon nitride ceramics *via* bond switching at coherent interfaces. *Science* 2022, **378**: 371–376.

[3] Meng Q, He G, Yang ZC, *et al.* Combustion synthesis of tunable-aspect-ratio β-Si_3N_4/BN composite ceramic materials. *J Am Ceram Soc* 2024, **107**: 7966–7972.

[4] Du SM, Li F, Zhang J, *et al.* Effects of sintering additives and sintering methods on the mechanical, antimicrobial and optical properties of Si_3N_4 bioceramics. *J Mech Behav Biomed Mater* 2024, **154**: 106529.

[5] Rice RW. Correlation of machining-grain-size effects on tensile strength with tensile strength–grain-size behavior. *J Am Ceram Soc* 1993, **76**: 1068–1070.

[6] Li CW, Lui SC, Goldacker J. Relation between strength, microstructure, and grain-bridging characteristics in *in situ* reinforced silicon nitride. *J Am Ceram Soc* 1995, **78**: 449–459.

[7] Yang JF, Sekino T, Niihara K. Effect of grain growth and measurement on fracture toughness of silicon nitride ceramics. *J Mater Sci* 1999, **34**: 5543–5548.

[8] Becher PF, Sun EY, Plucknett KP, *et al.* Microstructural design of silicon nitride with improved fracture toughness: I, effects of grain shape and size. *J Am Ceram Soc* 1998, **81**: 2821–2830.

[9] Lu HH, Huang JL. Microstructure in silicon nitride containing β-phase seeding: Part I. *J Mater Res* 1999, **14**: 2966–2973.

[10] Lu HH, Huang JL. Microstructure in silicon nitride containing β-phase seeding: III, grain growth and coalescence. *J Am Ceram Soc* 2001, **84**: 1891–1895.

[11] Lu HH, Huang JL. Microstructure of silicon nitride containing β-phase seeds: II. *J Am Ceram Soc* 2002, **85**: 2331–2336.

[12] Mitomo M. *In-situ* microstructural control in engineering ceramics. *Key Eng Mater* 1998, **161–163**: 53–58.

[13] Wang WD, Yao DX, Liang HQ, *et al.* Improved thermal conductivity of β-Si_3N_4 ceramics through the modification of the liquid phase by using GdH2 as a sintering additive. *Ceram Int* 2021, **47**: 5631–5638.

[14] Wang WD, Yao DX, Liang HQ, *et al.* Effect of *in-situ* formed Y_2O_3 by metal hydride reduction reaction on thermal conductivity of β-Si_3N_4 ceramics. *J Eur Ceram Soc* 2020, **40**: 5316–5323.

[15] Wang WD, Yao DX, Liang HQ, *et al.* Enhanced thermal conductivity in Si_3N_4 ceramics prepared by using ZrH_2 as an oxygen getter. *J Alloys Compd* 2021, **855**: 157451.

[16] Goto Y, Thomas G. Phase transformation and microstructural changes of Si_3N_4 during sintering. *J Mater Sci* 1995, **30**: 2194–2200.

[17] Kitayama M, Hirao K, Watari K, *et al.* Thermal conductivity of β-Si_3N_4: III, effect of rare-earth (RE = La, Nd, Gd, Y, Yb, and Sc) oxide additives. *J Am Ceram Soc* 2001, **84**: 353–358.

[18] Becher PF, Painter GS, Shibata N, *et al.* Effects of rare-earth (RE) intergranular adsorption on the phase transformation, microstructure evolution, and mechanical properties in silicon nitride with RE_2O_3+MgO additives: RE=La, Gd, and Lu. *J Am Ceram Soc* 2008, **91**: 2328–2336.

[19] Painter GS, Becher PF, Shelton WA, *et al.* First-principles study of rare-earth effects on grain growth and microstructure in β–Si_3N_4 ceramics. *Phys Rev B* 2004, **70**: 144108.

[20] Satet RL, Hoffmann MJ. Grain growth anisotropy of β-silicon nitride in rare-earth doped oxynitride glasses. *J Eur Ceram Soc* 2004, **24**: 3437–3445.

[21] Zhang Z, Duan XM, Zhang Z, *et al.* Effect of Re_2O_3–MgO additives on the microstructure evolution and properties of β-Si_3N_4 ceramics. *Ceram Int* 2021, **47**: 22073–22079.

[22] Du SM, Zhang J, Li F, *et al.* Effects of MgO-RE_2O_3 and SiO_2-RE_2O_3 (RE = La, Nd, Gd, Ho and Lu) complex sintering additives on the phase composition, microstructure and mechanical properties of dual-phase Si_3N_4 ceramics. *Ceram Int* 2023, **49**: 37922–37928.

[23] Sun LC, Tang YD, Cui Y, *et al.* On the fabrication and mechanical properties of Si_3N_4 ceramics with low content sintering additives. *Int J Appl Ceram Tec* 2023, **20**: 1269–1277.

[24] Liu W, Tong WX, Lu XX, *et al.* Effects of different types of rare earth oxide additives on the properties of silicon nitride ceramic substrates. *Ceram Int* 2019, **45**: 12436–12442.

[25] Becher PF, Shibata N, Painter GS, *et al.* Observations on the influence of secondary me oxide additives (Me = Si, Al, Mg) on the microstructural evolution and mechanical behavior of silicon nitride ceramics containing RE_2O_3 (RE = La, Gd, Lu). *J Am Ceram Soc* 2010, **93**: 570–580.

[26] Tatarko P, Lojanová Š, Dusza J, *et al.* Influence of various rare-earth oxide additives on microstructure and mechanical properties of silicon nitride based nanocomposites. *Mat Sci Eng A-Struct* 2010, **527**: 4771–4778.

[27] Nakashima Y, Zhou Y, Hirao K, *et al.* Processing strategy to trigger grain growth in silicon nitride. *J Am Ceram Soc* 2025, **108**: 20191.

[28] Wang WD, Pan Y, Zeng YP, *et al.* Effect of sintering aids content and powder characteristics on gas pressure sintered Si_3N_4 ceramics. *Ceram Int* 2024, **50**: 8260–8268.

[29] Guo WM, Yu JJ, Xiong M, *et al.* High-toughness Lu_2O_3-doped Si_3N_4 ceramics by seeding. *Ceram Int* 2016, **42**: 6495–6499.

[30] Jiang QG, Guo WM, Liu W, *et al.* Influence of powder characteristics on hot-pressed Si_3N_4 ceramics. *Sci Sintering* 2017, **49**: 81–89.

[31] Wang LJ, Qi Q, Cai P, *et al.* New route to improve the fracture toughness and flexural strength of Si_3N_4 ceramics by adding $FeSi_2$. *Scripta Mater* 2017, **126**: 11–14.

[32] Wang Q, Zhou CL, Yang C, *et al.* Analysis of friction and wear performance of Y_2O_3-doped Si_3N_4 ceramic using the estimation of stress. *Appl Phys A-Mater* 2023, **129**: 302.

[33] Liu MQ, Nemat-Nasser S. The microstructure and boundary phases of *in-situ* reinforced silicon nitride. *Mat Sci Eng A-Struct* 1998, **254**: 242–252.

[34] Senk MV, Mathias I, Zanotto ED, *et al.* Crystallized fraction and crystal size effects on the strength and toughness of lithium disilicate glass-ceramics. *J Eur Ceram Soc* 2023, **43**: 3600–3609.

[35] Liu CC, Chen QY, Sun P, *et al.* Synthesis of novel high-entropy diborides with high-efficiency electromagnetic wave absorption and excellent thermal stability. *J Adv Ceram* 2025, **14**: 9221030.

[36] Huang LP, Zhu JT, Liu JX, *et al.* Emerging high-entropy strategy: A booster to the development of cathode materials for power batteries. *J Adv Ceram* 2024, **13**: 1093–1118.

[37] Song WY, Lu YJ, Yang LT, *et al.* Enhancement of densification and mechanical property of $(Hf_{0.2}Zr_{0.2}Ti_{0.2}Nb_{0.2}Ta_{0.2})N$ high-entropy bulk ceramic via silicon carbide addition. *J Adv Ceram* 2025, **14**: 9221004.

[38] Wang WM, Liu BH, He CY, *et al.* High-entropy engineering for broadband infrared radiation. *Adv Funct Mater* 2023, **33**: 2303197.

[39] Wu RK, Wang QH, Wang XQ, *et al.* High-entropy $La(Al_{0.2}Co_{0.2}Fe_{0.2}Ni_{0.2}Cr_{0.2})O_{3-\delta}$ and $La(Al_{0.2}Co_{0.2}Fe_{0.2}Ni_{0.2}Mn_{0.2})O_{3-\delta}$ ceramics with broad-band high emissivity for long-term energy-saving. *J Mater Sci Technol* 2025, **234**: 122–133.

[40] Dong Y, Ren K, Lu YH, *et al.* High-entropy environmental barrier coating for the ceramic matrix composites. *J Eur Ceram Soc* 2019, **39**: 2574–2579.

[41] Zhi WK, Chen XY, Wang F, *et al.* Thermodynamic assessment of the CaO-Gd_2O_3–SiO_2 system. *Calphad* 2021, **75**: 102348.

[42] Li S, Shi JJ, Li D, *et al.* Thermodynamics study for Y_2O_3–Al_2O_3–SiO_2 system: Emphasis on the equilibrium phase relationship at 1400 and 1600 °C. *J Alloys Compd* 2025, **1026**: 180354.

[43] Costa GCC, Jacobson NS. Mass spectrometric measurements of the silica activity in the Yb_2O_3–SiO_2 system and implications to assess the degradation of silicate-based coatings in combustion environments. *J Eur Ceram Soc* 2015, **35**: 4259–4267.

[44] Ye XY, Luo Y, Liu SB, *et al.* Experimental study and thermodynamic calculation of Lu_2O_3–SiO_2 binary system. *J Rare Earth* 2017, **35**: 927–933.

[45] Zhi WK, Wang F, Chen XY, *et al.* Phase equilibria and thermodynamic assessment of the Al_2O_3–SiO_2–Sc_2O_3 system. *Ceram Int* 2023, **49**: 9735–9747.

[46] Hsu WL, Tsai CW, Yeh AC, *et al.* Clarifying the four core effects of high-entropy materials. *Nat Rev Chem* 2024, **8**: 471–485.

[47] Lu XX, Liu W, Li L, *et al.* Effects of MgO–Y_2O_3–Re_2O_3 on microstructure and properties of Si_3N_4 ceramics. *Mater Sci Eng Powder Metall* 2019, **24**: 536–541. (in Chinese)

[48] Cordero ZC, Knight BE, Schuh CA. Six decades of the Hall–Petch effect–A survey of grain-size strengthening studies on pure metals. *Int Mater Rev* 2016, **61**: 495–512.

[49] Park H, Kim HE, Niihara K. Microstructural evolution and mechanical properties of Si_3N_4 with Yb_2O_3 as a sintering additive. *J Am Ceram Soc* 1997, **80**: 750–756.

[50] Šajgalik P, Dusza J, Hoffmann MJ. Relationship between microstructure, toughening mechanisms, and fracture toughness of reinforced silicon nitride ceramics. *J Am Ceram Soc* 1995, **78**: 2619–2624.

[51] Shi YW, He QL, Wang AY, *et al.* Effect of additive content on texture evolution and mechanical properties of Si_3N_4 ceramics prepared by hot pressing. *Mat Sci Eng A-Struct* 2024, **898**: 146348.

[52] Han Y, Xie ZP, Li S, *et al.* Optimum sintering temperature of high quality silicon nitride ceramics under oscillatory pressure. *Ceram Int* 2018, **44**: 6949–6952.

[53] Ma BY, Tang YD, Deng CJ. Effects of Al_2O_3–Y_2O_3/Yb_2O_3 additives on microstructures and mechanical properties of silicon nitride ceramics prepared by hot-pressing sintering. *Int J Appl Ceram Tec* 2022, **19**: 2523–2532.

[54] Xiong H, Li B, Xi XA, *et al.* Preparation of graded silicon nitride ceramics with high mechanical performance using β-Si_3N_4 seeds. *Ceram Int* 2023, **49**: 36528–36535.

[55] Li YJ, Yang MH, Zhang YF, *et al.* A novel method of strong and tough Si_3N_4 ceramic from the particle-stabilized foam. *J Am Ceram Soc* 2023, **106**: 3832–3842.

[56] Lv XA, Li XH, Huang JW, *et al.* Effect of ultra-high pressure sintering and spark plasma sintering and subsequent heat treatment on the properties of Si_3N_4 ceramics. *Materials* 2022, **15**: 7309.

[57] Li ZH, Tong SY, Chen ZL, *et al.* Balancing mechanical properties of two-step spark plasma sintered Si_3N_4 ceramics by controlling pressure in the high-temperature step. *J Alloys Compd* 2025, **1037**: 182225.

[58] Wang LJ, Qi Q, Zhang H, *et al.* High tough W-added silicon nitride ceramics. *Ceram Int* 2019, **45**: 19055–19059.

[59] Deng K, Hu JB, Wei ZL, *et al.* Tailoring the thermal conductivity and mechanical properties of gas pressure sintered Si_3N_4 ceramics by changing nitrogen pressure. *Ceram Int* 2025, **51**: 39182–39192.

[60] Fu QL, Fu JX, Wang J, *et al.* Defects control of silicon nitride ceramics by oscillatory pressure sintering and consequent hot isotropic pressing. *Ceram Int* 2024, **50**: 3276–3280.